ACS NANO

www.acsnano.org

ARTICLE

Orbital Angular Momentum-Driven Ferromagnetism with Magnetic Anisotropy and Electronic Structure of Epitaxial Neodymium Nitride

Renuka Karanje, Anupam Bera, Sourav Rudra, Debmalya Mukhopadhyay, Souvik Banerjee, Manisha Bansal, Kiran Baraik, Sourav Chowdhury, Weibin Li, Manuel Valvidares, Tuhin Maity, and Bivas Saha*

Cite This: https://doi.org/10.1021/acsnano.5c11890 **Read Online**

ACCESS | Metrics & More | Article Recommendations | Supporting Information

ABSTRACT: Neodymium-based permanent magnets are fundamental to modern technologies, underpinning high-performance applications in electronics, renewable energy, and advanced medical systems. Among emerging neodymium compounds, neodymium nitride (NdN) has attracted significant attention due to its unique electronic structure, where strongly localized 4*f* orbitals and strong spin−orbit coupling are anticipated to drive exceptional magnetic behavior. Here, we show conclusive experimental evidence of orbital angular momentum-driven ferromagnetic ordering and prominent magnetic anisotropy in epitaxial, near-stoichiometric NdN thin films synthesized using ultrahigh vacuum deposition techniques. Magnetization and X-ray magnetic circular dichroism measurements reveal a dominant 4*f* orbital moment of 5.14 μ_B, contributing to a total magnetic moment of 2.43 μ_B per formula unit at 4 K, close to the first-principles density functional theory calculated values. Complementary synchrotron-radiation photoelectron spectroscopy, along with the theoretical calculations, uncovers occupied 4*f* states ~6.4 eV below the Fermi level, contributing to the orbital-driven ferromagnetism in NdN. Moreover, the high crystalline quality of the NdN films is further supported by the structural characterization and vibrational properties. The intrinsic orbital angular momentum-driven magnetism of NdN positions it as a promising platform for next-generation orbitronic devices beyond conventional spintronics.

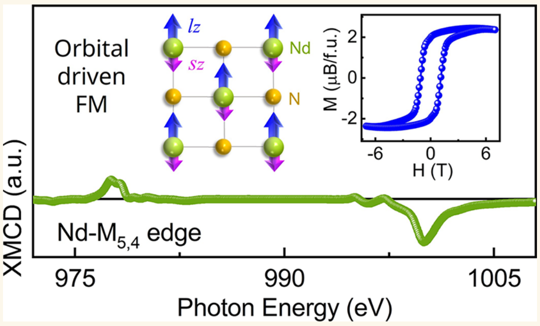

KEYWORDS: *orbital angular momentum, ferromagnetism, rare-earth nitrides, spin−orbit coupling, XMCD, SR-UPS, first-principles calculations*

INTRODUCTION

Neodymium permanent magnets are fundamental to modern technology, delivering exceptional magnetic performance essential for consumer electronics, renewable energy, and medical imaging applications.[1,2] Their remarkable strength stems from the intricate interplay of neodymium's localized 4*f* electrons, crystal field effects, and strong spin−orbit coupling (SOC), which collectively enhance magnetic moments and coercivity.[3−5] These materials also exhibit unique magnetic properties with significant potential for spintronics and high-performance magnetic devices.[3,5−8] However, beyond conventional NdFeB alloys, neodymium-based compounds such as neodymium nitride (NdN) have emerged as promising materials in recent years.[5,7−9] As a member of the lanthanide nitride family, NdN crystallizes in a cubic rock-salt structure and demonstrates narrow bandgap semiconducting behavior.[10] Unlike other rare-earth nitrides (RENs) such as SmN, EuN, and YbN, where rare earths exhibit partial divalent character, neodymium in NdN remains exclusively in the trivalent oxidation state, imparting distinct electronic and magnetic characteristics.[3,11,12] However, despite its potential, the development of NdN as the next generation magnetic and

Received: July 15, 2025
Revised: October 6, 2025
Accepted: October 6, 2025

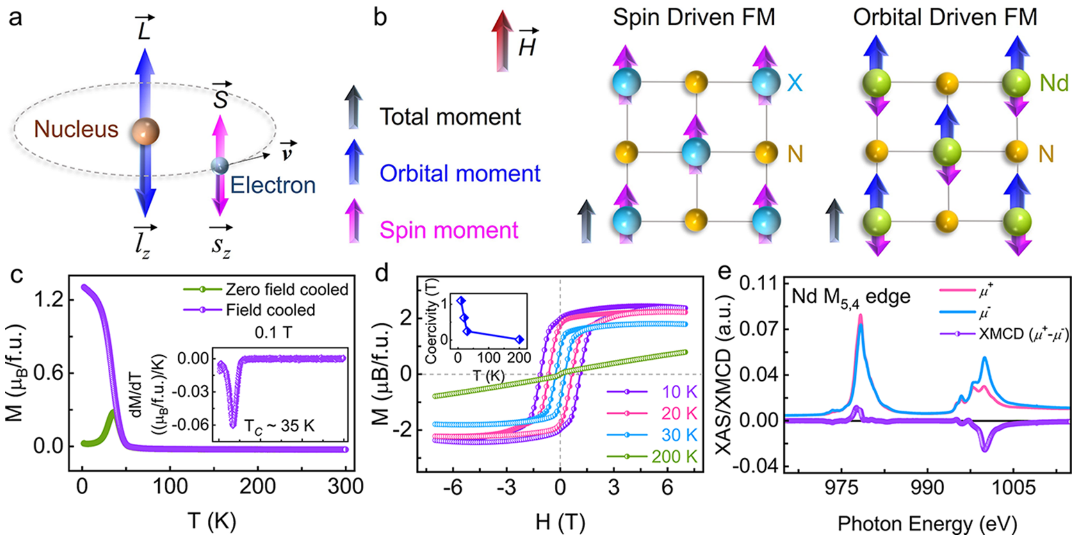

Figure 1. Orbital angular moment-driven ferromagnetism in NdN thin films. (a) Schematic illustration of orbital angular momentum resulting from electron motion around the nucleus and spin magnetic moment arising from the intrinsic quantum properties of electrons. (b) Nitride rock-salt structure highlighting spin-driven and orbital-driven contributions to ferromagnetism (FM). In pnictides such as XN, where X is a *3d* transition metal, the magnetism arises primarily from the spin angular moment, as the orbital contribution is largely quenched. In contrast, *4f* rare-earth systems like NdN, both spin and orbital angular momentum contribute significantly to magnetism. (c) Temperature-dependent field-cooled (FC) and zero-field-cooled (ZFC) out-of-plane magnetization of NdN at an applied field of 0.1 T. Inset shows derivative of field-cooled magnetization highlighting a T_C at ∼ 35 K. (d) Magnetization vs applied magnetic field measurement showing hysteresis loops of an NdN thin film deposited on (0001) Al_2O_3 substrate at various temperatures. The diamagnetic background from the substrate is subtracted for each temperature. The inset shows the temperature dependence of the coercive field. (e) X-ray Absorption Spectroscopy (XAS) and X-ray magnetic circular dichroism (XMCD) at the Nd-$M_{5,4}$ edges, demonstrating an orbital-driven net magnetic moment in NdN.

spintronic material has been hindered by challenges in synthesizing high-quality, stoichiometric bulk crystals and epitaxial thin films, primarily due to its extreme sensitivity to oxidation and the formation of undesired hydroxides.[13,14] Overcoming such growth challenges and understanding the intricate details of the electronic structure and magnetic ordering is crucial to unlocking NdN's full potential for next-generation applications.

In general, the magnetic properties of rare-earth pnictides are strongly governed by the unique behavior of partially filled *4f* orbitals, which fundamentally differ from the spin-dominated magnetism in *3d* transition metal compounds.[3,10,15−17] In conventional *3d* ferromagnetic systems, crystal field interactions from the surrounding ligands typically suppress the angular momentum contribution of the *3d* orbitals. However, in RENs, the highly localized nature of *4f* electrons enables a significant orbital angular momentum contribution, leading to unconventional ferromagnetic behavior.[18] This ferromagnetism mainly arises from two primary sources - the orbital angular momentum associated with electron motion around the nucleus and the spin angular momentum, an intrinsic quantum property of electrons. The inter-relationship of these contributions can be conceptualized, as illustrated in Figure 1a, where the total magnetic moment results from the combination of both orbital and spin moments. In rare-earth elements, SOC allows the orbital magnetic moment to remain significant even in the presence of the crystal field, as shown in Figure 1b.[18] According to Hund's rule, in heavy rare-earth elements, the spin and orbital momentum are parallel ($J = L + S$), which amplifies the total magnetic moment. In contrast, for light rare-earths like Nd, the spin and orbital momentum align antiparallel ($J = |L - S|$), so the orbital moment can oppose the spin moment, resulting in a negative net magnetization.[8,18,19] Such a notable phenomenon deviates from conventional spin-only magnetism, underscoring the complex magnetic nature of RENs and raising the possibility of devices that utilize a new subfield of orbitronics, where the presence of a large orbital magnetic moment can be used to generate long-range orbital torques.[20] Indeed, orbital angular momentum-driven ferromagnetic ordering has been an intense topic of research for NdN and SmN.[8,19]

In the case of NdN, early investigations date back to the 1960s, when sintered powders and bulk polycrystals were synthesized to explore their fundamental magnetic properties.[15] Resistivity and specific heat measurements as a function of temperature revealed a metallic-like positive temperature coefficient of resistivity, characteristic of many RENs.[21,22] Such behavior was attributed to the nitrogen vacancies (V_N) and substitutional oxygen at N-site (O_N) forming substoichiometric compositions, which commonly introduce heavy *n*-type doping in III-nitrides.[21] Optical absorption studies further confirmed the semiconducting nature of stoichiometric NdN, identifying a bandgap of ∼ 0.8 eV.[23] Previously reported, polycrystalline and powdered NdN exhibited a paramagnetic to ferromagnetic transition at a Curie temperature (T_C) between 25 and 35 K.[15,24−26] The measured saturation ferromagnetic moment also varied from 1.8 μ_B to 3.1 μ_B per formula unit, depending on sample quality and stoichiometry.[26,27] Neutron diffraction studies further revealed that, unlike other neodymium pnictides (e.g., NdP, NdAs, NdSb), which exhibit an antiferromagnetic ground state, NdN adopts a simple ferromagnetic ordering, such as observed in gadolinium nitride (GdN).[28,29] However, unlike the ferromagnetism in GdN, which solely emanates from the spin angular momentum, the ferromagnetism in NdN is expected to be mainly governed by the orbital angular momentum from the partially filled 4*f* orbitals.[18] Yet, all of these early studies on NdN were conducted on samples with varying degrees of oxygen contamination, oxidized surfaces, and nitrogen deficiency, preventing a precise determination of the intrinsic properties of the stoichiometric NdN. Notably, no reports from this period described in detail the growth of epitaxial and single-crystalline NdN thin films, which are crucial for device applications.

Recent advancements in molecular beam epitaxy (MBE)-deposited NdN have reignited research interest in this material, particularly through the deposition of high-quality thin films.[8,22] While these films exhibited polycrystalline morphology, they demonstrated an optical bandgap of ∼ 0.9 eV and a reduced ferromagnetic moment of 1.0 μ_B, below the Hund's rule value of 3.27 μ per formula unit, due to strain.[8] This renewed exploration of NdN offers a fresh perspective on its magnetism and electronic structure, potentially unlocking new opportunities for integration into spintronic and orbitronic device technologies. Moreover, determination of the electronic structure of NdN, particularly its valence band, through photoemission measurements is crucial not only for deepening the understanding of its electronic properties but also for providing essential insights into the origin of its magnetic ordering. Therefore, motivated by the prospect of utilizing NdN in practical devices, in this work, we develop epitaxial and highly crystalline NdN thin films and study the intricate details of its orbital angular momentum-driven magnetism and electronic structure. With its large orbital angular momentum contribution and magnetic anisotropy, NdN provides an ideal platform for advancing orbitronics.

RESULTS AND DISCUSSION

Epitaxial NdN thin films of thickness ∼ 95 nm are deposited on (0001) Al_2O_3 and (111) MgO substrates with an ultrahigh vacuum magnetron sputtering at a base pressure of 1×10^{-9} Torr and 800 °C substrate temperature. To protect the NdN films from oxidizing, an AlN capping layer is deposited on the films in situ at the same deposition conditions. AlN acts as an oxidation-resistant material due to the formation of a thin native Al_2O_3 coating on its surface, which prevents further oxidation.[30] Details of the growth and characterization methods are presented in the methods and experimental procedures section and Supporting Information (SI) Section 1. The AlN-capped NdN film appears reddish black, due to its relatively lower optical bandgap of 1.1 eV, as shown in Figure S1 of the SI Section 2. Room-temperature Hall measurements (performed with a 2 nm AlN capping layer) reveal an electron mobility of 9.4 ± 1.0 $cm^2/V.s$ for NdN films deposited on (0001) Al_2O_3 substrates. Additionally, a large *n*-type carrier concentration of 1.4×10^{21} cm^{-3} is measured, mainly due to the presence of substitutional oxygen impurities and a small amount of V_N as shown in Figures S16 and S15, respectively. The primary source of oxygen incorporation in as-deposited NdN thin films is contamination of the Nd target and residual oxygen in the deposition chamber, as the film is capped with an in situ deposited AlN layer to protect it from further oxidation under atmospheric humidity. Moreover, the presence of a small quantity of nitrogen vacancy in our NdN films cannot be ruled out and its presence also leads to an *n*-type doping nature in NdN (see Figure S15) similar to the O_N. Such a large carrier concentration results in a room-temperature resistivity of 4.5×10^{-4} Ω.cm in NdN, indicating its degenerate semiconductor behavior.

Field-cooled (FC) and zero-field-cooled (ZFC) magnetization measurements as a function of temperature with 0.1 T (see Figure 1c) out-of-plane applied magnetic field reveal a gradual increase in the magnetic moment starting from ∼ 50 K with a clear bifurcation between the ZFC and FC curves at ∼ 35 K, marking the onset of the phase transition from paramagnetic to ferromagnetic ordering. The temperature derivative of the FC magnetization (see inset in Figure 1c) additionally shows a prominent peak near 35 K, which corresponds to the ferromagnetic Curie temperature (T_C). The measured T_C of 35 K in NdN thin films agrees well with previously reported values on powder specimens but is slightly lower than the previous report on polycrystalline film.[8,15] Since V_N typically increases the T_C in RENs, the observed magnetization and T_C measurements suggest that our NdN films are nearly stoichiometric and contain minimal V_N.[31]

Temperature-dependent magnetization (M) vs applied out-of-plane magnetic field (H) measurements on (0001) Al_2O_3 substrate show characteristic hysteresis loops in NdN thin films below the T_C ∼ 35 K, confirming its robust ferromagnetic behavior (see Figure 1d). Hysteresis loops at 10, 20, and 30 K display distinct coercivity and remanent magnetization, providing clear evidence of a long-range ferromagnetic ordering. At 10 K, NdN thin films demonstrate a significant coercive field of 1.24 T, a high remanent magnetization of 2.03 μ_B, and a saturation magnetization of 2.37 μ_B per formula unit. Such out-of-plane magnetization is smaller than the ground state theoretical free-ion moment of 3.27 μ_B, calculated from the Hund's rule as $g_J\, \mu_B\, J$ with $J = 9/2$ for Nd^{3+} ions, where g_J, μ_B, and J represent the Landé g-factor, Bohr magneton, and total angular momentum of electrons, respectively. The out-of-plane magnetization is similar to the previously reported value of 2.15 μ_B per formula unit for powder NdN at 2 K and greater than 0.95 μ_B per formula unit for the thin film at 5 K.[8,15,22] Such a reduction in the saturation magnetic moment can be attributed to several factors, including partial quenching of orbital angular momentum by the crystal field, strong spin–orbit coupling that mixes spin and orbital contributions, residual strain in the thin film, and the presence of V_N.[7,8,28,32] The inset of Figure 1d shows the temperature dependence of the coercive field, which follows a typical ferromagnetic behavior, decreasing with temperature and sharply dropping above T_C due to the thermal perturbations. The magnetic measurement results of NdN on a (111) MgO substrate appear similar, with an out-of-plane saturation magnetic moment of 1.56 μ_B per formula unit and a T_C of ∼ 38 K. The magnetic data on the (111) MgO substrate are presented in SI Section 4.

To determine the precise orbital and spin magnetic moments contributions in NdN films, X-ray absorption spectroscopy (XAS) and X-ray magnetic circular dichroism (XMCD) measurements are performed at 4 K under an applied magnetic field of 6 T perpendicular to the incoming beam using total electron yield (TEY) mode with 3 nm AlN capping layer (see Figure 1e and Section 3 in SI for details).[33] By applying the sum-rule analysis to the XMCD data, the orbital magnetic moment (l_Z) and spin magnetic moment (s_Z) were quantitatively determined.[34−36] These analysis yields a l_Z of -5.14 μ_B and a s_Z of 2.98 μ_B, which sum up to a net magnetic moment of -2.16 μ_B per formula unit, in good agreement with density functional theory (DFT) calculated values of l_Z of −5.53 μ_B and a s_Z of 2.87 μ_B, resulting in a total magnetic moment of −2.66 μ_B per formula unit. This value closely matches the experimentally measured saturation magnetization at 10 K, confirming that the orbital contributions primarily govern the magnetic properties of NdN. The Nd-$M_{5,4}$ edges in the XAS spectra correspond to electronic transitions from the Nd-3*d* core levels to unoccupied 4*f* states. The observed splitting of the M_5 and M_4 peaks is attributed to the strong SOC within the Nd-3*d* core level. The XMCD spectra exhibit a pronounced dichroic signal, particularly at the $M_{5,4}$ edge, which signifies the dominance of the orbital component of the highly localized 4*f* electrons.

Along with the interesting ferromagnetic behavior, NdN thin films exhibit a distinct magnetic anisotropy (see Figure 2a, 2b, and 2c) that arises predominantly from the interaction of the localized 4*f* electrons of Nd^{3+} ions with the crystal field environment, a characteristic feature of RENs.[37,38] The highly localized 4*f* electrons interact strongly with the electrostatic potential of the surrounding ions in the cubic crystal structure, leading to a preferential alignment of the magnetic moments along specific crystallographic directions.[37] The NdN film grown on (0001) Al_2O_3 exhibits a higher out-of-plane magnetic moment per Nd atom than the in-plane moment. In contrast, the film deposited on (111) MgO shows nearly identical in-plane and out-of-plane moments (see Figures S3a and S3b), highlighting the crucial role of epitaxy and crystallographic orientation in governing the magnetic anisotropy. On (0001) Al_2O_3, NdN grows with a single out-of-plane (001) orientation but forms three twisted in-plane rotational domains (see Figure 5b and Figure S9), aligning Nd moments along the out-of-plane direction for all domains and enhancing the perpendicular magnetization while the in-plane magnetization is distributed across multiple rotational domains, and vector averaging reduces the net in-plane moment. On (111) MgO, the film shows a single growth orientation and no rotational domains, yielding comparable in-plane and out-of-plane moments. In addition, both the NdN films deposited on (0001) Al_2O_3 and (111) MgO substrates exhibit shape anisotropy that originates from the magnetostatic (dipolar) interaction associated with the geometry (shape) of the film with its characteristics like other magnetic thin films. Thus, the substrate-dependent epitaxy dictates the observed magnetic anisotropy also reported previously in Gd-substituted SmN.[39]

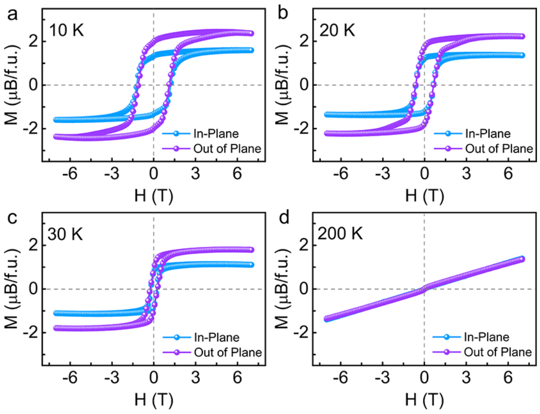

Figure 2. In-plane and out-of-plane magnetic anisotropy of NdN thin film at different temperatures. Magnetic field (H) dependence of magnetization (M) for NdN thin films measured at temperatures of (a) 10 K, (b) 20 K, (c) 30 K, and (d) 200 K. Below the Curie temperature (T_C) (10 to 30 K), a clear magnetic anisotropy is observed, where the out-of-plane magnetization exhibits a significantly higher magnetic moment compared to the in-plane configuration. In contrast, at 200 K, above T_C, both in-plane and out-of-plane magnetization curves overlap, indicating a transition to the paramagnetic phase. The out-of-plane magnetization results from Figure 1d are included here to better represent magnetic anisotropy.

Such magnetic anisotropy was not observed in previously reported polycrystalline NdN films, as these mixed orientations disrupt the uniform crystal field environment.[8] This highlights the critical role of epitaxial growth in determining the magnetic properties of NdN thin films. The oblate shape of the Nd^{3+} 4*f* electron cloud with slightly higher magnetic moment further facilitates shape anisotropy,[38] leads to an in-plane easy axis of sputtered deposited NdN thin films on both (0001) Al_2O_3 and (111) MgO substrates.

Additionally, the strong SOC in Nd enhances the anisotropic behavior.[38] In NdN, the spin and orbital angular momentum are coupled to form a total angular momentum, where the orbital contribution dominates the magnetic moment. This dominance stems from the large unquenched orbital angular moment value of Nd ions (Nd^{3+}), as evidenced by the larger magnetic moment in the out-of-plane direction compared to the in-plane configuration at 10, 20, and 30 K (Figures 2a-2c).[17,40] In contrast, at 200 K (Figure 2d), thermal fluctuation surpasses the exchange interaction, leading to the disordering of magnetic moments and the transition to a paramagnetic state. This is reflected in the overlapping magnetization curves for in-plane and out-of-plane orientations in the paramagnetic regime, indicating the absence of magnetic anisotropy above T_C. Such behavior distinguishes NdN from 3*d* transition metals, where the magnetic moment is predominantly spin-driven, and highlights the unique interplay of fundamental interactions in rare-earth materials. As a result, such orbital-moment-driven ferromagnetism in NdN offers a direct coupling to orbital currents, providing an efficient pathway for orbital torque switching. This positions NdN as a promising orbital Hall material (OHM) for next-generation orbitronic devices, enabling ultrafast and energy-efficient magnetization control. Furthermore, when integrated into heterostructures with 2D materials,[41,42] topological insulators, or ferroelectrics, NdN has the potential to drive highly efficient orbital torque-induced magnetization switching, opening new opportunities for advanced device applications.

To understand the microscopic origin of NdN's magnetism, the valence band (VB) electronic structure is measured using synchrotron-radiation ultraviolet photoelectron spectroscopy (SR-UPS) with an incident photon energy of 145.7 eV after complete removal of the AlN capping layer through Ar^+ ion sputtering at 1 keV. Figure 3a highlights the Nd-4*f*, Nd-5*d*, N-2*p*, O-2*p*, N-2*s*, Nd-5*p*, O-2*s*, and Nd-5*s* states along with the VB edge of NdN. The UPS spectrum is further compared with the electronic density of states of both the pristine and oxygen-doped NdN, calculated using the generalized-gradient approximation (GGA) with Hubbard-U corrections to both the Nd-5*d* and Nd-4*f* orbitals together.[43,44] Comparison of the calculated DOS with the measured VB spectrum reveals that without the Hubbard-U correction, the Nd-4*f* states appear near the Fermi edge (E_F), and significantly overlap with the Nd-5*d* and N-2*p* states near the VB maximum (see Figure 3bi),

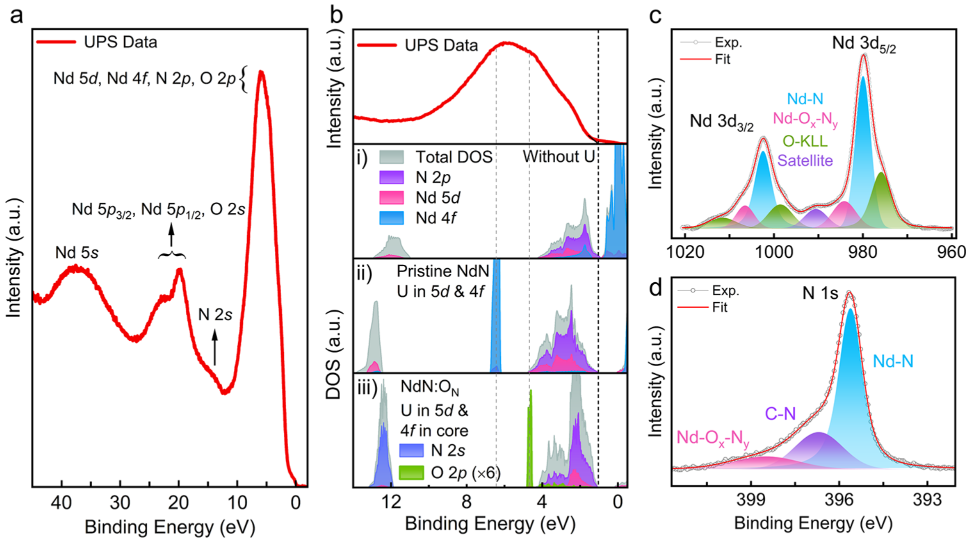

Figure 3. Experimental valence band profile and core level XPS spectra of NdN thin film. (a) Synchrotron-radiation ultraviolet photoelectron spectroscopy (SR-UPS) measurement of a NdN thin film after removing the top 10 nm AlN capping layer, revealing the valence band electronic structure. (b) The valence band electronic structure highlights the position of Nd-4*f* and O-2*p* inside the valence band, along with the hybridized Nd-5*d* and N-2*p* states. The vertical dotted line represents the valence band edge. Electronic density of states (DOS) of NdN for both with and without U correction are presented. Hubbard-U values of 6.6 and 5.0 eV were applied to the Nd-4*f* and Nd-5*d* orbitals, respectively. Additional calculations for oxygen-doped NdN with a U value of 7 eV for Nd-5*d* states, and considering Nd-4*f* as core electrons, showing the O-2*p* position inside the valence band. The Fermi level is set to zero, and the calculated valence band edge aligns well with the experimental SR-UPS spectra. c) The XPS core-level spectra of the NdN thin film, showing Nd-3$d_{3/2}$ and 3$d_{5/2}$ peaks along with the oxygen Auger peaks. d) The XPS core-level spectrum corresponding to the N-1*s* state, showing a prominent Nd−N bond.

underscoring the limitations of standard DFT in accurately capturing strong correlation effects of 4*f* electrons.

The small peak in the SR-UPS spectrum with binding energy of ∼ 2.6 eV corresponds to the N-2*p* states, as shown in Figure 3bii. Considering the strong correlation of 4*f* and 5*d* orbitals through Hubbard-U correction of 5 eV in Nd-5*d* and 6.6 eV in Nd-4*f* states, the occupied 4*f* states are positioned at ∼ 6.4 eV below the E_F, in good agreement with the intense peak of SR-UPS data as shown in Figure 3bii. However, as rare earths are prone to oxidation, a small amount of oxygen impurity could be present in the film. As a result, the electronic density of states (DOS) is further calculated, including a small amount (∼ 3.1%) of substitutional O_N, revealing their *n*-type doping nature with E_F inside the conduction band and the position of O-2*p* states at ∼ 4.7 eV below E_F. This matches well with the second observed peak in the SR-UPS spectrum, as shown in Figure 3biii, broadening the experimental VB spectrum. The position of O-2*p* does not shift significantly with increasing oxygen concentration, as shown in Figure S16. However, the thermal and instrumental broadening also contribute to the overall broadening of the experimental VB and corresponding orbitals as compared to the DFT-calculated, quite sharp projected DOS. Furthermore, the V_N point defect states appear inside the bandgap with *n*-type doping behavior, as shown in Section 8 of the SI. A detailed assessment of the doping nature of O_N and V_N in NdN, whether they act as shallow or deep defects, using charged defect formation energy calculations is yet to be performed and will be addressed in our future work.

X-ray photoelectron spectroscopy (XPS) using monochromatic Al K_α radiation is further employed to determine the chemical states of Nd and N in the thin films. Before XPS measurement, the 5 nm AlN capping layer was removed via Ar^+ ion sputtering at 1 keV to ensure accurate surface composition analysis. The binding energy (BE) positions are calibrated using the C-1*s* peak at 284.8 eV as a reference.[45] The XPS core-level spectra were deconvoluted into subpeaks using the Voigt function to identify contributions from different chemical states. The Nd-3*d* core level exhibits a characteristic spin−orbit splitting into the 3$d_{5/2}$ and 3$d_{3/2}$ components. Each of these components was further deconvoluted into two subpeaks. The 3$d_{5/2}$ subpeaks were observed at 981.3 and 985.5 eV, corresponding to Nd−N and Nd−O_x−N_y species, respectively. Similarly, the 3$d_{3/2}$ subpeaks were positioned at 1003.7 and 1007.8 eV.[45,46]

Since no literature is available for the precise Nd-3*d* binding energy in NdN, the observed peaks at 981.3 eV (3$d_{5/2}$) and 1003.7 eV (3$d_{3/2}$) are attributed to Nd bonded with nitrogen. The higher binding energy peaks at 985.5 and 1007.8 eV are assigned to oxynitride contributions, consistent with previous reports having an oxynitride peak at the higher BE side of Er-4*d* in ErN and other nitrides.[47,48] The higher atomic number of Nd (Z = 60) leads to strong SOC, resulting in a separation of 22.4 eV between 3$d_{5/2}$ and 3$d_{3/2}$, further consistent with the separation of the Nd-$M_{5,4}$ edge in XAS (see Figure 1e). Additionally, Auger O-*KLL* peaks were detected at 977.2, 999.7, and 1013.3 eV, indicating electron transfer from oxygen to the Nd-4*f* orbitals, further supporting the presence of Nd−O bonds as shown in Figure 3c.[45,46] The satellite peak observed at 991.9 eV does not overlap significantly with the main 3*d* core levels.[49] The N-1*s* core level spectrum was deconvoluted into three subpeaks located at 395.6, 396.7, and 398.5 eV, attributed to Nd−N, C−N, and Nd−N_x−O_y bonding environments, respectively, as shown in Figure 3d.[47,48] The presence of native oxygen and carbon in NdN results from impurities in the source materials and the background impurities inside the deposition chamber.

The electronic structure of NdN is calculated by considering the strong correlation effect of both 4*f* and 5*d* orbitals of Nd using Hubbard-U corrections on both orbitals simultaneously, as implemented in the recent version of the Quantum

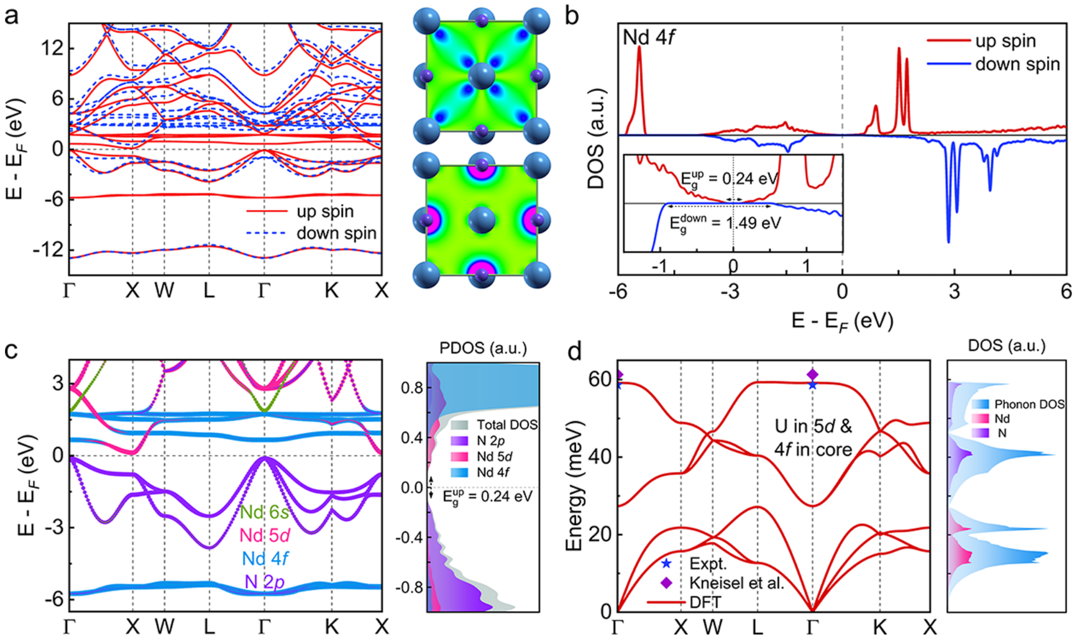

Figure 4. First-principles DFT+U calculated electronic structure and lattice dynamics of bulk NdN. (a) Electronic band structure of NdN calculated using GGA+U formalism with Hubbard-U values of 5.0 eV for Nd-5*d* and 6.6 eV for Nd-4*f* orbitals, showing the spin-resolved bands for up-spin (solid red) and down-spin (dashed blue) channels. The integrated local density of states from CBM to CBM + 100 meV and VBM to VBM − 100 meV are shown on the right-hand side, top and bottom, respectively. (b) Total DOS of NdN displaying clear spin polarization, with a distinct splitting between occupied and unoccupied 4*f* states, contributing to NdN's ferromagnetism. (c) Orbital-projected band structure and partial DOS for the up-spin channel of NdN, revealing hybridization between Nd-5*d* (pink), unoccupied Nd-4*f* (blue) near the X-point. The VB is majorly dominated by N-2*p* states, and a small Nd-6*s* contribution is present inside the CB at Γ. (d) Phonon dispersion of NdN, showing the splitting of longitudinal and transverse optical phonon modes (LO-TO) at the Γ-point, indicating NdN's polar dielectric behavior. The corresponding phonon density of states is shown on the right-hand side.

ESPRESSO package.[50] A Hubbard-U value of 5.0 eV for Nd-5*d* and 6.6 eV for Nd-4*f* states leads to a direct X-X band gap (E_g^{X-X}) of 0.91 eV and an indirect Γ-X band gap ($E_g^{\Gamma-X}$) of 0.24 eV for the up-spin channel. For the down-spin channel, such gaps are found to be 1.56 and 1.49 eV, respectively. Consequently, the average direct and indirect band gaps of NdN are calculated to be 1.23 and 0.86 eV, respectively, closely matching the experimental direct band gap in the room-temperature paramagnetic state (see Figure 5d).[27] Under the cubic crystal field, the 4*f* orbital splits into two 3-fold degenerate states, t_{2u} and t_{1u}, and a nondegenerate a_{2u} state.[18] In the up-spin configuration, a hybridization occurs between the unoccupied a_{2u} 4*f* states and 5*d* states of Nd near the conduction band minima at X (see Figure 4a), leading to the 4*f* electron-dominated large anomalous Hall effect in NdN, as observed previously.[18,51] However, such hybridization is weak for the down-spin channel, as shown in Figure 4a. The charge density plot of the conduction band minima (CBM) and valence band maxima (VBM) reveals Nd-5d_{xy} contribution at CBM and N-2*p* contribution in VBM.

The electronic DOS shows a spin-splitting between the occupied and unoccupied Nd-4*f* states, with the occupied 4*f* orbitals deep inside the valence band contributing to the magnetic moment of NdN (see Figure 4b). The projected density of states for the up-spin channel further confirms the hybridization between Nd-5*d* (pink color) and unoccupied Nd-4*f* (blue color) states near the CBM, along with a dominating N-2*p* (violet color) contribution in the valence band. A small contribution from Nd-6*s* (green color) is present inside the conduction band at the Γ-point, as shown in Figure 4c. Furthermore, SOC is included to determine the orbital and spin magnetic moments using the Vienna *Ab initio* Simulation Package (VASP),[52] resulting in a 4*f* orbital moment of −5.53 μ_B and corresponding spin moment of 2.87 μ_B, leading to a total ferromagnetic moment value of −2.66 μ_B per formula unit, in good agreement with the experimental XMCD data and previous theoretical study (see Section 8 in SI for more details).[18] However, the oxygen impurities present in the film would not significantly impact NdN's magnetic properties since the magnetic moments in NdN arise solely from Nd^{3+} ions and the O-2*p* orbitals are fully occupied in the O^{2-} state with zero magnetic moment. As a result, a small oxygen incorporation in terms of substitutional oxygen in nitrogen sites is unlikely to alter the magnetic properties of NdN.

The polar dielectric nature of NdN is further reflected in the calculated phonon dispersion spectrum (see Figure 4d), which exhibits a longitudinal and transverse optical phonon mode splitting at the Γ-point, highlighting the presence of Fröhlich interaction.[53−55] The highest LO phonon frequency at the Γ-point is ∼ 59 meV, which agrees well with the experimental Raman spectrum (see Section 9 of the SI) and previous literature.[9] However, no cation-vacancy-related peaks are observed in our sputtered-deposited NdN film, as observed in the recent report on ion-grown NdN films (see SI Section 9 and Figure S20).[56] A comparison of LO phonon with other rare-earth nitrides and similar rocksalt ScN is shown in Figure S21. Further, DFPT calculation shows that NdN exhibits an electronic dielectric constant (ε^{∞}) of 8.58 and the Born effective charge (Z^*) of ± 3.89*e* for the Nd and N atoms, respectively.[57]

Finally, structural characterization with symmetric 2*θ*-*ω* high-resolution X-ray diffractogram (HRXRD) exhibits a single

(002) oriented growth of NdN thin film on (0001) Al_2O_3 substrate (see Figure 5a) with an out-of-plane epitaxial relationship of (001) [001] NdN ∥ (0001) [0001] Al_2O_3. From the 2θ-peak position, an out-of-plane lattice constant of 5.14Å is determined, which matches well with previous literature reports.[8] Although the out-of-plane epitaxy is clear from the 2θ-ω scan, the in-plane epitaxial relationship is slightly complicated. The pole-figure measurement corresponding to the NdN (111) diffraction plane exhibits 12 equally spaced diffraction spots of comparable intensity (see Figure 5b). This further confirms the presence of three twisted 4-fold symmetric rotational domains of the NdN (001) base-plane (see Figure S9 in Supporting Information) with three in-plane epitaxial relationships individual to each grain. This type of 4-fold-on-6-fold symmetric heteroepitaxy was also previously observed in another REN SmN deposited on hexagonal AlN at an elevated growth temperature.[58] Additionally, the presence of a slight axiotaxy nature can be inferred from the pole figure,[59] indicating a degree of texture and mosaicity in the film, consistent with the higher full-width-at-half-maxima (fwhm) in the rocking curve of the (002) plane, see Section 7 in SI and Figure S11.

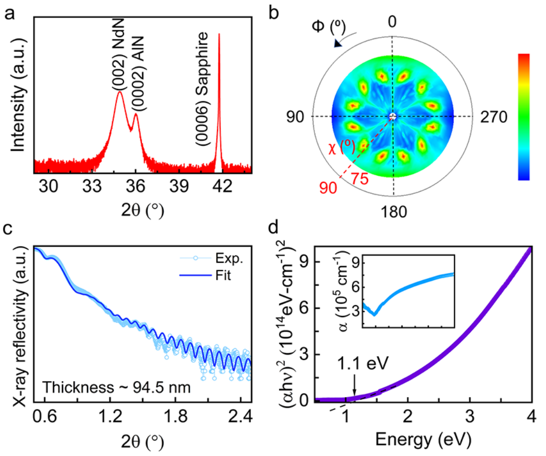

Figure 5. The structural and optical characterization of as-deposited epitaxial NdN thin film on (0001) Al_2O_3 substrate. (a) X-ray diffractogram of NdN thin film suggests epitaxial growth of a single (002) orientation on single-crystalline (0001) Al_2O_3 substrates. The diffraction peak from the ~ 30 nm AlN capping layer is also observed. (b) Pole-figure measurement of NdN corresponding to (111) reflection shows 12 equally spaced peaks, highlighting the three twisted 4-fold symmetric domains growth. (c) X-ray reflectivity (XRR) data and corresponding data fitting shows a NdN film thickness of 94.5 nm. (d) Tauc plot for NdN showing a direct optical bandgap of 1.1 eV. The inset shows the absorption coefficient (α) as a function of photon energy for the NdN thin film.

X-ray reflectivity (XRR) measurements show the Kiessig fringes, verifying layer coherency as shown in Figure 5c. Fitting of the XRR data provides a film thickness of ~ 94.5 nm, with an additional AlN capping layer thickness of 20 nm, and a surface roughness of approximately 1 nm. The obtained mass density of NdN from XRR analysis is 7.674 g/cm^3, in good agreement with the theoretical value of 7.67 g/cm^3. It suggests the suppression of nitrogen vacancy in the film, thus forming a near-stoichiometric NdN layer.

A direct optical bandgap of 1.1 eV was determined from the Tauc plot at room temperature in the paramagnetic phase (Figure 5d). This value is slightly higher than previously reported values (0.9−1.0 eV). The observed increase can be attributed to the Moss−Burstein effect, resulting from higher electron concentrations in our films compared to earlier studies.[8] In agreement with this, our theoretical calculations show the direct bandgap increasing from 0.82 eV in pristine NdN to 1.21 eV for both ~ 3.1% oxygen-doped and ~ 3.1% nitrogen-vacancy incorporated NdN, with the Fermi level lying inside the conduction band (Figures S18 and S15).

CONCLUSIONS

We report the conclusive experimental demonstration of orbital angular momentum-driven ferromagnetic ordering and magnetic anisotropy in epitaxial NdN thin films. Compared to the spin-dominated ferromagnetism typical of 3*d* transition metal systems, magnetism in NdN originates from highly localized 4*f* electrons, yielding a substantial orbital magnetic moment of 5.14 μ_B and a total moment of 2.37 μ_B per formula unit, which is slightly below the theoretical limit. Synchrotron-radiation photoelectron spectroscopy further reveals the position of the 4*f* orbitals and provides detailed insights into the valence band structure. First-principles DFT calculations further corroborate these findings, consistently capturing both magnetic and electronic behavior. With its significant orbital contribution, strong spin−orbit coupling, and tunable ferromagnetic properties, NdN emerges as a promising platform for new generation orbitronics, enabling novel strategies to manipulate orbital currents for quantum information technologies, advanced data storage devices, and spintronics applications.

METHODS AND EXPERIMENTAL PROCEDURES

Thin Film Growth. NdN thin films, protected by an AlN capping layer, are deposited on 1 cm × 1 cm (0001)-oriented Al_2O_3 and (111)-oriented MgO substrates using reactive DC magnetron sputtering (PVD Products, Inc.) within an ultrahigh vacuum sputtering chamber with a base pressure of 1 × 10^{-9} Torr. Before deposition, the substrates underwent ultrasonic cleaning in acetone and methanol for 8 min each. The Nd sputtering target, with a purity of 99.9% and dimensions of 2 in. in diameter and 0.25 in. in thickness, was presputtered for several hours to eliminate surface contaminations and oxide layers. During the film growth, Ar:N_2 gas mixture was maintained at a flow ratio of 9:2 standard cubic centimeters per minute (SCCM), and the chamber pressure was stabilized at 5 mTorr. The deposition was performed at a constant power of 100 W, with the substrate temperature of 800 °C. The AlN capping layer was deposited using a high-purity (99.999%) Al target under the same growth conditions.

Measurements & Characterizations. Magnetic measurements were performed using a SQUID-based MPMS (Quantum Design, USA), recording hysteresis loops up to 7 T in the 10−300 K range. XMCD spectra at the Nd−$M_{5,4}$ edges and N−K edge were measured in the TEY mode at 4 K under a 6 T field at the BOREAS beamline, ALBA Synchrotron (Spain), using a grazing incidence setup with a 20° sample angle and varying beam helicity. UPS measurements were carried out at the BL-10 beamline, Indus-2 (RRCAT, India), after removing the AlN capping layer via 1 keV Ar$^+$ sputtering for 60 min. Valence band spectra were recorded at room temperature using an incident energy of 145.7 eV and calibrated with Au foil, maintaining a vacuum of ~9 × 10^{-11} mbar. HRXRD was carried out using a Rigaku SmartLab diffractometer (Cu−K$_\alpha$, λ=1.54 Å) with parallel beam optics. Pole figure measurements were performed in Bragg−Brentano mode by varying χ from 0−75°, and XRR fitting was done using Parratt formalism in SmartLab software.

Detailed Computational Methodology. The first principle DFT calculation implemented in the Quantum ESPRESSO and VASP software was used for electronic band structure, DOS, and phonon dispersion calculations. Both GGA and HSE06 hybrid functionals are used with the PAW pseudopotentials for Nd and N atoms.[60,61] The plane-wave basis cutoff energy was set to 140 eV in Quantum ESPRESSO. The Γ-centered Brillouin zone was sampled using an 8 × 8 × 8 k-point mesh for the HSE calculations and a 16 × 16 × 16 k-point mesh for the GGA calculations, based on a 2-atom primitive unit cell of NdN. The nonlocal Hartree−Fock exchange mixing parameter in the HSE calculation was set to 0.35 to obtain a band gap close to the experimental value. The phonon dispersion of NdN was calculated using the finite displacement method, as implemented in the Phonopy code.[62] A 2 × 2 × 2 supercell containing 64 atoms was used in this calculation. The PBE parametrized GGA exchange-correlation functional was used with a plane-wave energy cutoff of 600 eV. The PAW pseudopotential with Nd-4f electrons as core was used for the phonon calculation, as accurately capturing the room-temperature electronic bandgap of NdN is not possible in VASP by considering both 5d and 4f orbitals of Nd in the pseudopotential while applying the Hubbard-U correction to only one of those orbitals. As a result, a Hubbard-U correction of 7.0 eV was applied to the Nd-5d states to account for strong electronic correlations and bandgap correction close to the experimental value. The PAW pseudopotential with Nd-4f electrons as core was used for the phonon calculation. A Hubbard-U correction of 7.0 eV was applied to the Nd-5d states to account for strong electronic correlations and bandgap correction. The Brillouin zone integration was performed using a Γ-centered 8 × 8 × 8 k-point mesh.

ASSOCIATED CONTENT

Data Availability Statement

The data that support the findings of this study are available from the corresponding author upon reasonable request.

Supporting Information

The Supporting Information is available free of charge at https://pubs.acs.org/doi/10.1021/acsnano.5c11890.

> Details on the effect of AlN capping layer on NdN thin film, XMCD analysis, magnetic measurement on MgO (111) substrate, structural characterization, additional computational results, selection of the capping layers, and their influence on physical properties (PDF)

AUTHOR INFORMATION

Corresponding Author

Bivas Saha − *Chemistry and Physics of Materials Unit, Jawaharlal Nehru Centre for Advanced Scientific Research, Bangalore 560064, India; International Centre for Materials Science and School of Advanced Materials, Jawaharlal Nehru Centre for Advanced Scientific Research, Bangalore 560064, India;* orcid.org/0000-0002-0837-1506; Email: bsaha@jncasr.ac.in, bivas.mat@gmail.com

Authors

Renuka Karanje − *Chemistry and Physics of Materials Unit, Jawaharlal Nehru Centre for Advanced Scientific Research, Bangalore 560064, India; International Centre for Materials Science, Jawaharlal Nehru Centre for Advanced Scientific Research, Bangalore 560064, India*

Anupam Bera − *Chemistry and Physics of Materials Unit, Jawaharlal Nehru Centre for Advanced Scientific Research, Bangalore 560064, India; International Centre for Materials Science, Jawaharlal Nehru Centre for Advanced Scientific Research, Bangalore 560064, India*

Sourav Rudra − *Chemistry and Physics of Materials Unit, Jawaharlal Nehru Centre for Advanced Scientific Research, Bangalore 560064, India; International Centre for Materials Science, Jawaharlal Nehru Centre for Advanced Scientific Research, Bangalore 560064, India*

Debmalya Mukhopadhyay − *Chemistry and Physics of Materials Unit, Jawaharlal Nehru Centre for Advanced Scientific Research, Bangalore 560064, India; International Centre for Materials Science, Jawaharlal Nehru Centre for Advanced Scientific Research, Bangalore 560064, India*

Souvik Banerjee − *Chemistry and Physics of Materials Unit, Jawaharlal Nehru Centre for Advanced Scientific Research, Bangalore 560064, India; International Centre for Materials Science, Jawaharlal Nehru Centre for Advanced Scientific Research, Bangalore 560064, India*

Manisha Bansal − *School of Physics, Indian Institute of Science Education and Research Thiruvananthapuram, Thiruvananthapuram, Kerala 695551, India*

Kiran Baraik − *Synchrotrons Utilization Section, Raja Ramanna Centre for Advanced Technology, Indore 452013, India*

Sourav Chowdhury − *Deutsches Elektronen-Synchrotron DESY, Hamburg 22607, Germany*

Weibin Li − *ALBA Synchrotron Light Source, Cerdanyola del Vallès, Barcelona E-08290, Spain;* orcid.org/0009-0003-4037-113X

Manuel Valvidares − *ALBA Synchrotron Light Source, Cerdanyola del Vallès, Barcelona E-08290, Spain;* orcid.org/0000-0003-4895-8114

Tuhin Maity − *School of Physics, Indian Institute of Science Education and Research Thiruvananthapuram, Thiruvananthapuram, Kerala 695551, India;* orcid.org/0000-0003-4386-1006

Complete contact information is available at: https://pubs.acs.org/10.1021/acsnano.5c11890

Author Contributions

R.K. and B.S. conceived this project. R.K. deposited thin films and performed electrical and structural characterization. S.B, M.B., and T.M performed magnetic measurements. S.C., W.L., and M.V. performed XMCD/XAS measurement. R.K., S.R. and K.B. performed UPS measurement. A.B. and S.R. performed the theoretical modeling under the assistance of B.S. R.K., and D.M. performed the Optical measurement. All authors discussed and contributed to the preparation of the manuscript.

Notes

The authors declare no competing financial interest.

ACKNOWLEDGMENTS

R.K. and B.S. acknowledge the International Centre for Materials Science (ICMS) and Sheikh Saqr Laboratory (SSL) of Jawaharlal Nehru Centre for Advanced Scientific Research (JNCASR) for support. B.S. acknowledges the Anusandhan National Research Foundation (ANRF) in India for a Core Research Grant No. CRG/2023/007061 for financial support. A.B., S.R. and B.S. sincerely acknowledge the support and resources provided by PARAM Yukti Facility under the National Supercomputing Mission (NSM), Government of India, at the Jawaharlal Nehru Centre for Advanced Scientific Research (JNCASR), Bangalore. R.K. and D.M. thank JNCASR for the fellowship. A.B. acknowledges the University Grants Commission (UGC) for the fellowship. S.R. and S.B. acknowledge the Council of Scientific & Industrial Research (CSIR) for the fellowship. T.M. acknowledges the

SERB-SRG Project No. 2021/000423 and the Helium Plant funded by DST for magnetic measurements with the SQUID. XMCD measurements were carried out at the ALBA Synchrotron Light Source beamline, Barcelona, Spain (Proposal IHR2024028436 and IHR2025019055). M.V. acknowledges funding by the MCIN/AEI grant PID2023-146354NB-C43. R.K. acknowledges Ms. Mehek Loyal, Mr. Rahul Singh Rawat, and Dr. Dheemahi Rao for their valuable assistance during the experimental work.

REFERENCES

(1) Herbst, J. F.; Croat, J. J.; Pinkerton, F. E.; Yelon, W. B. Relationships between Crystal Structure and Magnetic Properties in Nd$_2$Fe$_{14}$B. *Phys. Rev. B* **1984**, *29* (7), 4176−4178.

(2) Sugiyama, J.; Miwa, K.; Nozaki, H.; Kaneko, Y.; Hitti, B.; Arseneau, D.; Morris, G. D.; Ansaldo, E. J.; Brewer, J. H. Magnetic Moment of Rare-Earth Elements in R$_2$Fe$_{14}$B Estimated with μ^+SR. *Phys. Rev. Mater.* **2019**, *3* (6), No. 064402.

(3) Natali, F.; Ruck, B. J.; Plank, N. O. V.; Trodahl, H. J.; Granville, S.; Meyer, C.; Lambrecht, W. R. L. Rare-Earth Mononitrides. *Prog. Mater. Sci.* **2013**, *58* (8), 1316−1360.

(4) Petukhov, A. G.; Lambrecht, W. R. L.; Segall, B. Electronic Structure of Rare-Earth Pnictides. *Phys. Rev. B* **1996**, *53* (8), 4324−4339.

(5) Aravindh, S. A.; Roqan, I. S. Structural, Magnetic and Electronic Properties of Two Dimensional NdN: An *Ab Initio* Study. *RSC Adv.* **2019**, *9* (61), 35917−35923.

(6) Aerts, C. M.; Strange, P.; Horne, M.; Temmerman, W. M.; Szotek, Z.; Svane, A. Half-Metallic to Insulating Behavior of Rare-Earth Nitrides. *Phys. Rev. B* **2004**, *69* (4), No. 045115.

(7) McNulty, J. F.; Anton, E.-M.; Ruck, B. J.; Suzuki, M.; Mizumaki, M.; Trodahl, H. J. Tunable Magnetic Exchange Springs in Semiconductor GdN/NdN Superlattices. *Phys. Rev. B* **2019**, *100* (9), No. 094441.

(8) Anton, E.-M.; McNulty, J. F.; Ruck, B. J.; Suzuki, M.; Mizumaki, M.; Antonov, V. N.; Quilty, J. W.; Strickland, N.; Trodahl, H. J. NdN: An Intrinsic Ferromagnetic Semiconductor. *Phys. Rev. B* **2016**, *93* (6), No. 064431.

(9) Kneisel, K.; Maddah, M.; Chan, J.; Xu, Y.; Casey-Stevens, C.; Van Koughnet, K.; Holmes-Hewett, W.; Trodahl, H. J.; Natali, F. Synthesis, Structural, and Raman Investigation of Lanthanide Nitride Powders (Ln = La, Ce, Nd, Sm, Gd, Tb, Dy, Er, Lu). *ACS Omega* **2024**, *9* (48), 47842−47847.

(10) Olcese, G. L. Interconfiguration Fluctuation of Cerium in CeN as a Function of Temperature and Pressure. *J. Phys. F Met. Phys.* **1979**, *9* (3), 569−578.

(11) Richter, J. H.; Ruck, B. J.; Simpson, M.; Natali, F.; Plank, N. O. V.; Azeem, M.; Trodahl, H. J.; Preston, A. R. H.; Chen, B.; McNulty, J.; Smith, K. E.; Tadich, A.; Cowie, B.; Svane, A.; van Schilfgaarde, M.; Lambrecht, W. R. L. Electronic Structure of EuN: Growth, Spectroscopy, and Theory. *Phys. Rev. B* **2011**, *84* (23), No. 235120.

(12) Holmes-Hewett, W. F.; Miller, J. D.; Ahmad, H. G.; Granville, S.; Ruck, B. J. Rare-Earth Nitrides: Fundamental Advances and Applications in Cryogenic Electronics. *J. Phys. D. Appl. Phys.* **2025**, *58* (34), No. 343001.

(13) Eick, H. A.; Baenziger, N. C.; Eyring, L. The Preparation, Crystal Structure and Some Properties of SmN, EuN and YbN 1. *J. Am. Chem. Soc.* **1956**, *78* (23), 5987−5989.

(14) van Dover, R. B.; Schneemeyer, L. F.; Gyorgy, E. M. Magnetic Properties of Gd-Substituted Yttrium Nitride. *MRS Proc.* **1986**, *89*, No. 147.

(15) Schumacher, D. P.; Wallace, W. E. Magnetic Characteristics of Some Lanthanide Nitrides. *Inorg. Chem.* **1966**, *5* (9), 1563−1567.

(16) Hulliger, F. Magnetic Properties of the Rare Earth Pnictides. *J. Magn. Magn. Mater.* **1978**, *8* (3), 183−205.

(17) Meyer, C.; Ruck, B. J.; Preston, A. R. H.; Granville, S.; Williams, G. V. M.; Trodahl, H. J. Magnetic Properties of ErN Films. *J. Magn. Magn. Mater.* **2010**, *322* (14), 1973−1978.

(18) Larson, P.; Lambrecht, W. R. L.; Chantis, A.; van Schilfgaarde, M. Electronic Structure of Rare-Earth Nitrides Using the LSDA+U Approach: Importance of Allowing 4*f* Orbitals to Break the Cubic Crystal Symmetry. *Phys. Rev. B* **2007**, *75* (4), No. 045114.

(19) Meyer, C.; Ruck, B. J.; Zhong, J.; Granville, S.; Preston, A. R. H.; Williams, G. V. M.; Trodahl, H. J. Near-Zero-Moment Ferromagnetism in the Semiconductor SmN. *Phys. Rev. B* **2008**, *78* (17), No. 174406.

(20) Wang, P.; Chen, F.; Yang, Y.; Hu, S.; Li, Y.; Wang, W.; Zhang, D.; Jiang, Y. Orbitronics: Mechanisms, Materials and Devices. *Adv. Electron. Mater.* **2025**, *11* (5), No. 2400554.

(21) Sclar, N. Properties of Rare-Earth Nitrides. *J. Appl. Phys.* **1964**, *35* (5), 1534−1538.

(22) Van Koughnet, K.; Holmes-Hewett, W. F.; Ruck, B. J. Enhanced Magnetic Remanence and Electron Mobility in (100)-Epitaxial NdN Thin Films. *J. Appl. Phys.* **2025**, *138* (6), No. 065102.

(23) Wachter, P. Physical Properties of Some Stoichiometric Rare Earth Nitride Single Crystals. *Adv. Mater. Phys. Chem.* **2015**, *05* (03), 96−131.

(24) van der Kraan, A. M.; Buschow, K. H. J. Magnetic Properties of Rare Earth Compounds of the Type RFe$_4$Al$_8$. *Phys. B+C* **1977**, *86*, 93−94.

(25) Veyssie, J. J.; Chaussy, J.; Berton, A. Chaleurs Specifiques Du Nitrude de Lanthane et Du Nitrude de Neodyme. *Phys. Lett.* **1964**, *13* (1), 29−30.

(26) Junod, P.; Menth, A.; Vogt, O. Revue Des Propriétés Magnétiques et Électroniques Des Composés Des Terres Rares Avec Les Anions Du 5ième Groupe Du Système Périodique. *Phys. der Kondens. Mater.* **1969**, *8* (5), 323−370.

(27) Gschneidner, K.; Eyring, L.; Lander, G. *Handbook on the Physics and Chemistry of Rare Earths*; North Holland Publishing Company: 1979. Vol. *44*.

(28) Schobinger-Papamantellos, P.; Fischer, P.; Vogt, O.; Kaldis, E. Magnetic Ordering of Neodymium Monopnictides Determined by Neutron Diffraction. *J. Phys. C Solid State Phys.* **1973**, *6* (4), 725−737.

(29) Leuenberger, F.; Parge, A.; Felsch, W.; Fauth, K.; Hessler, M. GdN Thin Films: Bulk and Local Electronic and Magnetic Properties. *Phys. Rev. B* **2005**, *72* (1), No. 014427.

(30) Loyal, M.; Biswas, B.; Das, P.; Saha, B. Coexistence of Infrared Plasmon and Thermoelectricity in Rare-Earth Semiconducting Ytterbium Nitride. *Appl. Phys. Lett.* **2023**, *123* (4), No. 042101.

(31) Plank, N. O. V.; Natali, F.; Galipaud, J.; Richter, J. H.; Simpson, M.; Trodahl, H. J.; Ruck, B. J. Enhanced Curie Temperature in N-Deficient GdN. *Appl. Phys. Lett.* **2011**, *98* (11), No. 112503.

(32) Furrer, A.; Halg, W. Crystal-Field Splittings of NdN and HoN. *J. Phys. C Solid State Phys.* **1976**, *9* (18), 3499−3505.

(33) Barla, A.; Nicolás, J.; Cocco, D.; Valvidares, S. M.; Herrero-Martín, J.; Gargiani, P.; Moldes, J.; Ruget, C.; Pellegrin, E.; Ferrer, S. Design and Performance of BOREAS, the Beamline for Resonant X-Ray Absorption and Scattering Experiments at the ALBA Synchrotron Light Source. *J. Synchrotron Radiat.* **2016**, *23* (6), 1507−1517.

(34) Xu, D. B.; Sun, C. J.; Chen, J. S.; Heald, S. M.; Sanyal, B.; Rosenberg, R. A.; Zhou, T. J.; Chow, G. M. Large Enhancement of Magnetic Moment in $L1_0$ Ordered FePt Thin Films by Nd Substitutional Doping. *J. Phys. D. Appl. Phys.* **2015**, *48* (25), No. 255001.

(35) Tripathi, S. XMCD Investigation at M4, 5 Edges of the Rare Earth Elements in High-Performance Permanent Magnet. Thesis, Max-Planck-Institut für Intelligente Syst. Stuttgart, **2018**, 176.

(36) Chowdhury, S.; Jana, A.; Kuila, M.; Reddy, V. R.; Choudhary, R. J.; Phase, D. M. Negative Charge-Transfer Energy in SrCoO$_{2.5}$ Thin Films: An Interplay between O-2p Hole Density, Charge-Transfer Energy, Charge Disproportionation, and Ferromagnetic Ordering. *ACS Appl. Electron. Mater.* **2020**, *2* (12), 3859−3870.

(37) Skomski, R.; Sellmyer, D. J. Anisotropy of Rare-Earth Magnets. *J. Rare Earths* **2009**, *27* (4), 675−679.

(38) Skomski, R.; Kashyap, A.; Enders, A. Is the Magnetic Anisotropy Proportional to the Orbital Moment? *J. Appl. Phys.* **2011**, *109* (7), No. 07E143.

(39) Miller, J. D.; Trodahl, H. J.; Al Khalfioui, M.; Vézian, S.; Ruck, B. J. Unlocking Perpendicular Magnetic Anisotropy with Gd Substitution in SmN. *Appl. Phys. Lett.* **2023**, *122* (9), No. 092402.

(40) Boldrin, D.; Johnson, F.; Thompson, R.; Mihai, A. P.; Zou, B.; Zemen, J.; Griffiths, J.; Gubeljak, P.; Ormandy, K. L.; Manuel, P.; Khalyavin, D. D.; Ouladdiaf, B.; Qureshi, N.; Petrov, P.; Branford, W.; Cohen, L. F. The Biaxial Strain Dependence of Magnetic Order in Spin Frustrated Mn_3NiN Thin Films. *Adv. Funct. Mater.* **2019**, *29* (40), No. 1902502.

(41) Chen, Y.; Chen, C.; Kealhofer, R.; Liu, H.; Yuan, Z.; Jiang, L.; Suh, J.; Park, J.; Ko, C.; Choe, H. S.; Avila, J.; Zhong, M.; Wei, Z.; Li, J.; Li, S.; Gao, H.; Liu, Y.; Analytis, J.; Xia, Q.; Asensio, M. C.; Wu, J. Black Arsenic: A Layered Semiconductor with Extreme In-Plane Anisotropy. *Adv. Mater.* **2018**, *30* (30), No. 1800754.

(42) Zhang, J.; Chen, S.; Du, G.; Yu, Y.; Han, W.; Xia, Q.; Jin, K.; Chen, Y. Experimental Observation of Highly Anisotropic Elastic Properties of Two-Dimensional Black Arsenic. *Nano Lett.* **2023**, *23* (19), 8970−8977.

(43) Perdew, J. P.; Burke, K.; Ernzerhof, M. Generalized Gradient Approximation Made Simple. *Phys. Rev. Lett.* **1996**, *77* (18), 3865−3868.

(44) Dudarev, S. L.; Botton, G. A.; Savrasov, S. Y.; Humphreys, C. J.; Sutton, A. P. Electron-Energy-Loss Spectra and the Structural Stability of Nickel Oxide: An LSDA+U Study. *Phys. Rev. B* **1998**, *57* (3), 1505−1509.

(45) Briggs, D. X. *Handbook of Adhesion*; Wiley: 2005; p 261.

(46) Talik, E.; Kruczek, M.; Sakowska, H.; Ujma, Z.; Gała, M.; Neumann, M. XPS Characterisation of Neodymium Gallate Wafers. *J. Alloys Compd.* **2004**, *377* (1−2), 259−267.

(47) Upadhya, K.; Kumar, R.; Baral, M.; Tripathi, S.; Jha, S. N.; Ganguli, T.; Saha, B. Electronic Structure of Rare-Earth Semiconducting ErN Thin Films Determined with Synchrotron Radiation Photoemission Spectroscopy and First-Principles Analysis. *Phys. Rev. B* **2022**, *105* (7), No. 075138.

(48) Shukla, N.; Rudra, S.; Karanje, R.; Mukhopadhyay, D.; Das, P.; Biswas, B.; Baral, M.; Gupta, M.; Saha, B. Strain-Induced Valence Band Splitting Enabling Above-Bandgap Exciton Luminescence in Epitaxial Mg_3N_2 Thin Films. *Chem. Mater.* **2024**, *36* (11), 5563−5573.

(49) LIU, X.; LI, M.; YANG, S.; YANG, Y.; NIE, J.; XUE, Y.; OUYANG, Y.; XIAO, S. High-Performance Scavenging of Nd (III) and Sm (III) from Water by a Copper-Based Metal-Organic Framework HKUST-1. *J. Chem. Sci.* **2022**, *134* (3), 68.

(50) Giannozzi, P.; Baroni, S.; Bonini, N.; Calandra, M.; Car, R.; Cavazzoni, C.; Ceresoli, D.; Chiarotti, G. L.; Cococcioni, M.; Dabo, I.; Dal Corso, A.; de Gironcoli, S.; Fabris, S.; Fratesi, G.; Gebauer, R.; Gerstmann, U.; Gougoussis, C.; Kokalj, A.; Lazzeri, M.; Martin-Samos, L.; Marzari, N.; Mauri, F.; Mazzarello, R.; Paolini, S.; Pasquarello, A.; Paulatto, L.; Sbraccia, C.; Scandolo, S.; Sclauzero, G.; Seitsonen, A. P.; Smogunov, A.; Umari, P.; Wentzcovitch, R. M. QUANTUM ESPRESSO: A Modular and Open-Source Software Project for Quantum Simulations of Materials. *J. Phys.: Condens. Matter* **2009**, *21* (39), No. 395502.

(51) Holmes-Hewett, W. F.; Buckley, R. G.; Ruck, B. J.; Natali, F.; Trodahl, H. J. 4*f* Conduction in the Magnetic Semiconductor NdN W. *Phys. Rev. B* **2019**, *100* (19), No. 195119.

(52) Kresse, G.; Furthmüller, J. Efficient Iterative Schemes for *Ab Initio* Total-Energy Calculations Using a Plane-Wave Basis Set. *Phys. Rev. B* **1996**, *54* (16), 11169−11186.

(53) Van Koughnet, K.; Trodahl, H. J.; Holmes-Hewett, W. F.; Ruck, B. J. Defect-Activated versus Intrinsic Raman Spectra of GdN and LuN. *Phys. Rev. B* **2023**, *108* (6), No. 064306.

(54) Giustino, F. Electron-Phonon Interactions from First Principles. *Rev. Mod. Phys.* **2017**, *89* (1), No. 015003.

(55) Rudra, S.; Rao, D.; Poncé, S.; Saha, B. Dominant Scattering Mechanisms in Limiting the Electron Mobility of Scandium Nitride. *Nano Lett.* **2024**, *24* (37), 11529−11536.

(56) Markwitz, M.; Van Koughnet, K.; Kneisel, K.; Holmes-Hewett, W. F.; Natali, F.; Trewick, E. X. M.; Porteous, L.; Ruck, B. J.; Trodahl, H. J. Raman Signatures of Cation Vacancies in Rare Earth Nitrides. *Phys. Rev. B* **2025**, *112* (6), No. 064101.

(57) Baroni, S.; de Gironcoli, S.; Dal Corso, A.; Giannozzi, P. Phonons and Related Crystal Properties from Density-Functional Perturbation Theory. *Rev. Mod. Phys.* **2001**, *73* (2), 515−562.

(58) Chan, J. R.; Vézian, S.; Trodahl, J.; Khalfioui, M. A.; Damilano, B.; Natali, F. Temperature-Induced Four-Fold-on-Six-Fold Symmetric Heteroepitaxy, Rocksalt SmN on Hexagonal AlN. *Cryst. Growth Des.* **2016**, *16* (11), 6454−6460.

(59) Detavernier, C.; Özcan, A. S.; Jordan-Sweet, J.; Stach, E. A.; Tersoff, J.; Ross, F. M.; Lavoie, C. An Off-Normal Fibre-like Texture in Thin Films on Single-Crystal Substrates. *Nature* **2003**, *426* (6967), 641−645.

(60) Heyd, J.; Scuseria, G. E.; Ernzerhof, M. Hybrid Functionals Based on a Screened Coulomb Potential. *J. Chem. Phys.* **2003**, *118* (18), 8207−8215.

(61) Kresse, G.; Joubert, D. From Ultrasoft Pseudopotentials to the Projector Augmented-Wave Method. *Phys. Rev. B* **1999**, *59* (3), 1758−1775.

(62) Togo, A.; Chaput, L.; Tadano, T.; Tanaka, I. Implementation Strategies in Phonopy and Phono3py. *J. Phys.: Condens. Matter* **2023**, *35* (35), No. 353001.